Sustainable Energy & Fuels

ROYAL SOCIETY OF CHEMISTRY

PAPER

View Article Online
View Journal | View Issue

Cite this: *Sustainable Energy Fuels*, 2020, **4**, 4076

# High-energy and high-power Zn–Ni flow batteries with semi-solid electrodes†

Yun Guang Zhu, ‡[a] Thaneer Malai Narayanan, ‡[b] Michal Tulodziecki, [a] Hernan Sanchez-Casalongue,[d] Quinn C. Horn,[d] Laura Meda,[e] Yang Yu,[c] Jame Sun,[b] Tom Regier,[f] Gareth H. McKinley *[b] and Yang Shao-Horn *[abc]

Received 30th January 2020
Accepted 1st June 2020

DOI: 10.1039/d0se00675k

rsc.li/sustainable-energy

Flow battery technology offers a promising low-cost option for stationary energy storage applications. Aqueous zinc–nickel battery chemistry is intrinsically safer than non-aqueous battery chemistry (*e.g.* lithium-based batteries) and offers comparable energy density. In this work, we show how combining high power density and low-yield stress electrodes can minimize energy loss due to pumping, and have demonstrate methods to achieve high energy and power density for ZnO/Ni(OH)$_2$ electrodes by changing composition and optimizing testing protocols. Firstly, mechanically stable and homogeneous Ni(OH)$_2$/carbon and ZnO/Zn flowable electrodes in 7 M KOH electrolyte were designed using a microgel dispersion as the suspending matrix. By determining the critical volume fractions for conductivity percolation, colloidal suspensions with 6.2 vol% of carbon and 23.1 vol% of Zn were selected for preparing catholytes and anolytes to ensure that these semi-solid electrodes possess high voltage and high coulombic efficiencies. The resulting flowable electrodes exhibited non-Newtonian rheology with a yield stress of approximately ∼200 Pa, which assists in maintaining mechanical stability of the suspensions. An energy density of up to 134 W h $\mathrm{L_{catholyte}}^{-1}$ and power density up to ∼159 mW $\mathrm{cm_{geo.}}^{-2}$ was demonstrated for semi-solid ZnO/Ni(OH)$_2$ electrodes, and coulombic efficiency of 94% was achieved during cycling by optimizing the charging protocol to 60% SOC of Ni(OH)$_2$. Lastly, semi-solid ZnO and Ni(OH)$_2$ flow cells were built and tested using an intermittent mode of operation. The high energy and power densities, high coulombic efficiency, and negligible pumping loss of the Zn–Ni semi-solid electrodes developed in the present work present a promising system for further development.

## Introduction

With the increase of energy consumption and greenhouse gas emission, the role of renewable energy sources such as solar and wind energy has become more significant.[1] As energy generation by these sources is intermittent daily and can vary seasonally, safe and reliable energy storage systems are necessary to meet our grid energy demands.[2–4] Unlike commonly used pumped hydro,[5] electrochemical energy storage systems store much greater energy per unit volume, thus incurring fewer geographic restrictions.[6] Flow batteries have decoupled energy and power in contrast to Li-ion batteries with coupled energy and power, which are deemed as one of the most promising storage technologies for grid-scale applications.[7] Unfortunately, currently-available flow batteries have energy densities (on a per volume basis) lower than Li-ion batteries.[8] This is because flow battery electrodes (either catholyte or anolyte) have lower densities of redox centers per electrode volume due to limited solubility of active redox molecules (*e.g.* solubilities are limited to ∼1 M for 9,10-anthraquinone-2,7-disulphonic acid (AQDS),[9] ∼2 M for $VO^{2+}$ in acid[10]).[8,11] For example, the vanadium redox flow battery (VRFB) employs vanadium redox molecules with four different oxidation states to provide a practical energy density of ∼40 W h $\mathrm{L_{catholyte}}^{-1}$ on the system level.[10,12] Unfortunately, the cost of this stored energy is high due to high cost of vanadium and Nafion® membrane, which is used to separate the anolyte and catholyte. Recently, a large number of new redox molecules has been reported to lower the cost and/or enhance energy per volume.[13] Low-cost organic redox molecules have been examined in flow batteries, such as quinone species[14,15] (*e.g.* 0.5 M 2,6-dihydroxyanthraquinone with 0.4 M $K_4Fe(CN)_6$,

---

[a] *Research Laboratory of Electronics, Massachusetts Institute of Technology, 77 Massachusetts Avenue, Cambridge, MA 02139, USA. E-mail: shaohorn@mit.edu*

[b] *Department of Mechanical Engineering, Massachusetts Institute of Technology, 77 Massachusetts Avenue, Cambridge, MA 02139, USA. E-mail: gareth@mit.edu*

[c] *Department of Material Science and Engineering, Massachusetts Institute of Technology, 77 Massachusetts Avenue, Cambridge, MA 02139, USA*

[d] *Exponent Inc, 1075 Worcester St, Natick, MA 01760, USA*

[e] *Dipart. Chimica-Fisica, Istituto Eni Donegani, Centro Recerche per Rinnovabili e Ambiente, Italy*

[f] *Canadian Light Source Inc., Saskatoon, Saskatchewan S7N 0X4, Canada*

† Electronic supplementary information (ESI) available. See DOI: 10.1039/d0se00675k

‡ These authors contributed equally.

having ~11 W h $L_{catholyte}^{-1}$), ferrocene/viologen[16] (2.0 M BTMAP-Vi with 1.9 M BTMAP-Fc, having ~40 W h $L_{catholyte}^{-1}$), phenazine species[17] (1.4 M 7,8-dihydroxyphenazine-2-sulfonic acid with 0.4 M $K_4Fe(CN)_6$, having ~15 W h $L_{catholyte}^{-1}$). In addition, redox-targeting flow batteries have been shown to have increased energy densities by storing solid active material in the tank and shuttling redox mediator species between the tank and cell stack.[18–21] For example, a design employing 10-methylphenothiazine and 9-fluorenone to assist $Na_3V_2(PS_4)_3$-based redox flow battery chemistry has resulted in energy densities up to 176 W h $L_{catholyte}^{-1}$.[21] However, these flow batteries with soluble redox species are prone to cross-over of redox molecules through the membrane, resulting in coulombic efficiencies that are much lower than Li-ion batteries, even with the use of high-cost ion-selective membranes[22] (*e.g.* Nafion membranes with the cost of US$ 200 per $m^2$). To further increase stored energy and eliminate high-cost ion-exchange membranes, semi-solid flowable electrodes, which consist of solid active particles dispersed in the electrolyte, have been introduced.[4,23,24] Several types of semi-solid flow batteries have been successfully demonstrated such as Li–S (>400 W h $L_{catholyte}^{-1}$)[25] and $Li_4Ti_5O_{12}$–$LiCoO_2$ (ref. 26) (~800 W h $L_{catholyte}^{-1}$, theoretical value) where non-aqueous electrolyte is used. The non-aqueous electrolyte can be expensive (*e.g.* carbonate electrolyte US$ 14 per kg)[27] increasing the cost of the semi-solid electrode. Very recently, an aqueous $LiTi_2(PO_4)_3$–$LiFePO_4$ flow battery has been reported but the volumetric energy density reported is low, ~40 W h $L_{catholyte}^{-1}$.[4] A zinc/nickel system formulated from Zn/ZnO and $Ni(OH)_2$/NiOOH is reported to have high volumetric energy density of 128 W h $L_{catholyte}^{-1}$ (achieved 14 W h $L_{catholyte}^{-1}$), but the achieved power density (2.7 mW $cm_{geo.}^{-2}$) is exceptionally low,[28] compared to ~100 mW $cm_{geo.}^{-2}$ for VRFB,[29] ~65 mW $cm_{geo.}^{-2}$ for $LiTi_2(PO_4)_3$–$LiFePO_4$ (ref. 21) and ~14 mW $cm_{geo.}^{-2}$ for Li–S.[25] While semi-solid flowable electrodes can, in principle, provide volumetric energy densities considerably greater than soluble redox electrode chemistry, realizing the energy gain at reasonable power and over extensive cycling remains a major challenge, which can be attributed to more complex design considerations of semi-solid flowable electrodes.

In this work, we aim to develop aqueous semi-solid flowable electrodes and battery chemistry with substantially enhanced volumetric energy densities and areal power densities to those reported to date. Semi-solid flowable electrodes typically consist of solid active materials in addition to conductive particles (*e.g.* carbon black) which reduce electric resistance of the electrodes. The conductive particles form a stress-bearing network of interparticle contacts among the attractively-interacting particles, which can confer gel-like non-Newtonian flow properties to semi-solid flowable electrodes.[30–32] The physical and chemical properties of the semi-solid flowable electrodes govern the energy density, power density, efficiency and cycling life of the flow battery; however, the systematic optimization of these properties is not straightforward. Increasing the volume fraction of the conductive additive can increase the electronic conductivity and battery power density but this can be at the expense of the flowability and sedimentational stability of the semi-solid flowable electrode and can increase the pumping energy loss associated with transporting the anolyte and catholyte. Typical semi-solid flowable electrodes are dense suspensions and can be referred to generically as yield stress fluids. The formulated slurry only flows when the attractive force between the suspended particles is overcome (*i.e.* at macroscopic stresses above a yield stress $\tau_y$[31,32]). The viscoplastic nature of these semi-solid electrodes can potentially lead to higher power requirements for pumping than when using soluble redox molecules (liquid only). Therefore, correlating flowable electrode compositions with electrical properties, flow characteristics and electrochemical performance are key to systematically design semi-solid flowable electrodes with high energy and power densities.

Here we focus on aqueous Zn–Ni battery chemistry to design a semi-solid flow battery that demonstrates both high energy and power densities. Among reported aqueous flow battery chemistries (VRFB,[11] Fe–Cr,[33] BTMAP-Fc/Vi,[16] Zn–$Br_2$,[34] LTP–LFP[a],[4] Zn–$I_2$/$Br_2$,[35] Zn–$I_2$[a],[39] PS-$Br_2$,[36] DHAQ–$K_4Fe(CN)_6$,[14] and AQDS–HBr[9]), Zn–Ni semi-solid flow battery chemistry can exhibit the highest energy density (~240 W h $L_{catholyte}^{-1}$ for 12.5 vol% of $Ni(OH)_2$), as shown in Fig. 1. Zn–Ni battery chemistry is known to have a high equilibrium voltage (~1.8$V_{cell}$, Fig. S1†), which is much higher than aqueous $LiTi_2(PO_4)_3$–$LiFePO_4$ (~1.0 V).[4] In addition, by using a 3D Zn sponge anode, Parker *et al.* demonstrated a Zn–Ni static battery with high power and long lifetime.[37] Moreover, a Zn–$I_2$ hybrid flow battery[38] has shown high energy efficiency (81%) at a current density of 40 mA $cm_{geo.}^{-2}$. In this study, we focus on the design of semi-solid Zn-based anolyte and semi-solid $Ni(OH)_2$-based catholyte and their use in static cells and flow batteries. The volume percentages of active materials, ZnO and $Ni(OH)_2$ respectively, together with conductive additives were first correlated with the measured conductivity and yield stress of anolyte and catholyte. From these measurements, optimum

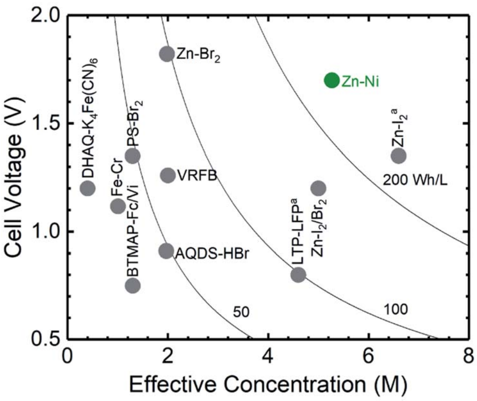

Fig. 1 Theoretical volume energy densities of some representative aqueous flow battery chemistries including VRFB,[11] Fe–Cr,[33] BTMAP-Fc/Vi,[16] Zn–$Br_2$,[34] LTP–LFP[a],[4] Zn–$I_2$/$Br_2$,[35] Zn–$I_2$[a],[38] PS-$Br_2$ (ref. 36) and DHAQ–$K_4Fe(CN)_6$,[14] and AQDS–HBr.[9] Abbreviations: BTMAP-Fc: 1,1′-bis[3-(trimethylammonio)propyl]ferrocene dichloride, BTMAP-Vi: bis(3-trimethylammonio)propyl viologen tetrachloride, PS: polysulfide, AQDS: 9,10-anthraquinone-2,7-disulphonic acid, DHAQ: 2,6-dihydroxyanthraquinone, LTP: $LiTi_2(PO_4)_3$, LFP: $LiFePO_4$.

flowable electrode compositions were determined, corresponding to <1% of battery power output consumed through mechanical energy dissipation during pumping. Subsequently, the volume percentages of $Ni(OH)_2$ and conductive additives were varied and correlated to changes in the electrochemical performance of the system, including the volumetric energy density, areal power density, voltage efficiency and coulombic efficiency. Static cells with optimized ZnO and $Ni(OH)_2$ semi-solid flowable electrode formulations were shown to reach high energy densities (up to 134 W h $L_{catholyte}{}^{-1}$), high power densities (up to 159 mW $cm_{geo.}{}^{-2}$) and high coulombic efficiencies of up to 92%. Finally, the suitability of the semi-solid electrodes for a flow battery application was demonstrated.

## Results and discussion

### Electronic percolation of semi-solid electrodes

The electronic percolation threshold for the semi-solid anolyte and catholyte was first determined in order to design electrodes that provide sufficiently high electron-conducting pathways throughout the suspension.[39,40] The percolation threshold was defined as the critical volume fraction $\Phi_c$ at which a sharp increase in the conductivity was observed.[41] Theoretically, below $\Phi_c$, only small clusters of conductive particles exist, whereas, at $\Phi_c$, at least one "infinitely" large sample-spanning cluster of conductive particle gives rise to a sharp increase in conductivity. Above $\Phi_c$, the extent of this sample-spanning cluster grows and the volume of unconnected void space within the semi-solid electrode shrinks. The electronic percolation threshold was found to be approximately 5.5 vol% for Zn (suspended in 93.4 vol% of KOH solution and 1.1 vol% of Carbopol microgel) and 2.5 vol% for Acetylene Black (or AB) (suspended in 96.6 vol% of KOH solution and 0.9 vol% of Carbopol gel). Above these volume fractions, the electronic conductivity remained nearly constant with increasing Zn or AB, as shown in Fig. 2a and b, respectively. In addition, the electronic conductivity of the suspension remained reasonably high upon the addition of less conductive active material particles of ZnO, where a conductivity up to ~80 mS $cm^{-1}$ was noted for an anolyte with 21.3 vol% of Zn and 8.1 vol% of ZnO. The conductivity of the Zn suspension first dramatically decreases with the addition of ZnO and then gradually rises again at higher volume fractions of ZnO. This observation is probably due to coverage of ZnO particles on Zn surface and improved alignment of the Zn with a further increase of ZnO respectively. Moreover, a conductivity of ~1 mS $cm^{-1}$ was maintained for a catholyte with 5.4 vol% of AB and increasing volume percentages of $Ni(OH)_2$ particles, up to 12.5 vol%, as shown in Fig. 2b right. These anolyte and catholyte compositions would result in a maximum energy density of 228 W h $L_{catholyte}{}^{-1}$ for Zn–Ni semi-solid flow batteries (assuming 1.7 V as the discharge voltage). Here, the

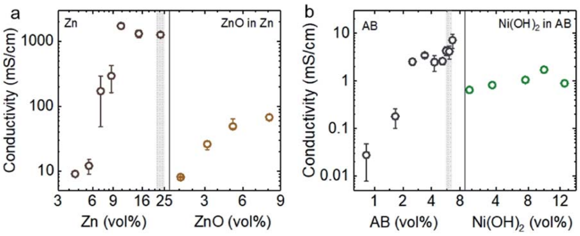

Fig. 2 (a) The conductivity of semi-solid electrodes with different volume percentages of Zn particles (Zn, 100–300 μm in size, Fig. S2a†), where the conductive percolation threshold was ~5.5 vol%, and the conductivity of anolyte (ZnO in Zn) as a function of volume fraction of ZnO (100–500 nm in size, Fig. S2c†) from 1.1 to 8.1%, accompanied with comparable volume percentages of Zn particles (21.3–22.9 vol%). (b) The conductivity of semi-solid electrodes with different volume percentages of acetylene black (AB, 50–100 nm in particle size, Fig. S2b†) only, where the conductive percolation threshold was ~2.5 vol%, and with different volume percentages of $Ni(OH)_2$ (10–30 μm in size, Fig. S2d†) with comparable percentages of AB (5.4–6.1 vol%). The detailed compositions of these suspensions are listed in Tables S1–S4.† The standard deviations were calculated from three independent measurements.

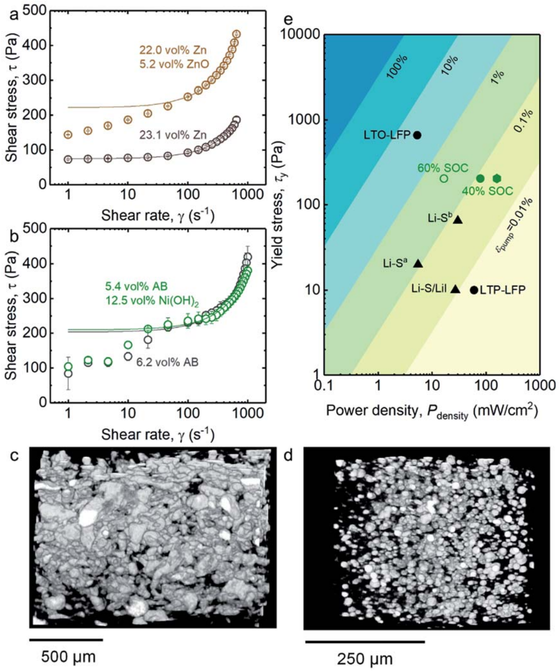

Fig. 3 (a) Flow curves of 23.1 vol% of Zn suspension (purple circles), and 22.0 vol% of Zn and 5.2 vol% of ZnO suspension (brown circles), respectively; (b) Flow curves of 6.2 vol% of AB suspension (grey circles) and 5.4 vol% of AB and 12.5 vol% of $Ni(OH)_2$ suspension (green circles), respectively. Shear stress was averaged over three measurements. The experimental data is fitted with the Bingham model to find an upper-bound estimate of the yield stress (solid lines) (all fitting parameters are listed in Tables S5–S8.†); (c) Three dimensional (3D) micro X-ray tomography of ZnO/Zn anolyte (8.1 vol% of ZnO and 21.3 vol% of Zn); (d) 3D micro X-ray tomography of $Ni(OH)_2$/AB catholyte (10.0 vol% of $Ni(OH)_2$ and 5.5 vol% of AB); (e) mechanical energy dissipation due to pumping calculated for a 1 kW flow battery stack with 30 parallel channels (details of calculation in ESI†). Thickness of each channel was set at 2 mm, channel width was set at 30 cm, and energy density of the flowable electrode was set at a nominal value of 100 W h $L_{catholyte}{}^{-1}$ to provide an order of magnitude of mechanical energy dissipation over energy output of the battery. For comparison, yield stress and power density values of semi-solid flow battery (circle) and semi-solid hybrid flow battery (triangle) reported in the literature (Li–S[a],[25] Li–S[b],[45] Li–S/LiI,[3] LTP–LFP,[4] LTO–LFP[24]) are also shown.

anolyte of 5.2 vol% ZnO and 22.0 vol% Zn has a greater theoretical volumetric capacity (268 A h $L_{anolyte}^{-1}$) than that of the catholyte, composed of 12.5 vol% $Ni(OH)_2$ and 5.4 vol% AB (134 A h $L_{catholyte}^{-1}$). This value is four-fold higher than that of the estimated maximum energy density for the VRFB shown in Fig. 1. The flow characteristics and electrochemical properties of these flowable electrodes will be discussed in the following sections.

### Flow characteristics of semi-solid anolyte and catholyte

The rheological characteristics of the semi-solid anolyte and catholyte with optimized conductivity (Fig. 2) were also measured, as shown in Fig. 3a and b, respectively. An upper-bound estimate of the yield stress for these semi-solid electrodes was obtained by fitting the experimental flow curve (circles) to the Bingham model (lines, refer to Tables S5–S8† for fitting parameters), from which a yield stress of 75 Pa was found for 23.1 vol% Zn electrode. This yield stress increases to 222 Pa upon the addition of 5.2 vol% colloidal ZnO in Fig. 3a. In addition, as shown in Fig. 3b, the yield stress of the 6.2 vol% AB catholyte was measured to be 204 Pa, which remained largely unchanged (209 Pa) upon the addition of 12.5 vol% $Ni(OH)_2$. The higher yield stress of the AB-only electrode compared to Zn-only electrode can be attributed to stronger interparticle attraction among the colloidal carbon black particles,[42] or among carbon black particles and polymer chains,[43] as well as to the fractal-like morphologies of the carbon black aggregates (Fig. S2b†). The increased yield stress in the anolyte upon addition of 5.2 vol% of ZnO could be attributed to the formation of attractive ZnO colloidal networks[31](Fig. S2c†). On the other hand, the comparable yield stress of the catholyte with, and without, the addition of 12.5 vol% $Ni(OH)_2$ (Fig. 3b) might be associated with the lack of long-range attraction among $Ni(OH)_2$ particles.

The high yield stress of suspensions like those that form the Zn/ZnO anolyte and AB/$Ni(OH)_2$ catholyte arise from the presence of stress-bearing particle networks which can also confer mechanical stability to these semi-solid flowable electrodes, preventing sedimentation of the large particles such as Zn and $Ni(OH)_2$.[41,44] The corresponding suspensions underwent rapid sedimentation without the inclusion of the Carbopol© microgel polymer in the electrolyte (Fig. S3†). Three-dimensional (3-D) micro X-ray tomography taken a month after suspension preparation reveals highly-stable and well-dispersed Zn and $Ni(OH)_2$ particles in the anolyte and catholyte as shown in Fig. 3c and d, respectively, which is necessary to achieve long calendar life of flow batteries.

The yield stress of Zn/ZnO anolyte and AB/$Ni(OH)_2$ catholyte used in this study is about the same order of magnitude as the LFP electrode employed in LTO–LFP work[24] and one order of magnitude higher than those electrodes reported in Li–$S^a$,[25] Li–$S^b$,[45] Li–S/LiI,[3] LTP–LFP.[4] This can be attributed to the following reasons. Firstly, the active particles used in this study were supplied in solid powder form, unlike the previously-reported work in which melted sulfur-carbon composite is used for Li-$S^{a25}$ and Li–S/LiI[3] batteries. Melted composite reduces the volume percentage of solid particles within the semi-solid electrode (∼2.2 vol% carbon for Li–$S^{a25}$ and Li–S/LiI,[3] assuming the density of carbon particles is 1.9 g $cm^{-3}$). Secondly, experimental precautions aimed at prevention of wall slip during flow curve measurements are not always taken, which could result in under-reporting of measured yield stresses.[31,32,45–48] While the high yield stress of the electrodes studied here enhances the electrode mechanical stability (Fig. 3c and d), it can also increase the power dissipated during pumping, which will be estimated below.

### Mechanical energy dissipation analysis for semi-solid flowable electrodes

The ratio of energy dissipated (per unit time) during pumping to the power output of the battery, denoted $\varepsilon_{pump}$ (Fig. 3e) was estimated using the upper-bound estimate of the yield stress determined by regression to the Bingham model (Fig. 3a and b),[24,46,49] and the maximum power density attainable with the electrode (Fig. 6). Details of this calculation are provided in the "Estimation of mechanical energy dissipation during pumping" section of the ESI.† The flow channel dimensions were assumed to be similar to conventional flow battery stacks, having a channel width of ∼30 cm, the number of parallel channels was set at 30, and the channel thickness was set at 2 mm. In addition, the calculation includes the following assumptions, the electrode was assumed to flow through the channel only once,[4,45] and the length of the channel was assumed to change to achieve the required area for 1 kW power output. As expected, decreasing the yield stress will lead to lower energy dissipated during pumping (Fig. 3e). Similarly, as the power density attainable with the semi-solid electrode increases, the fraction of the total energy dissipated during pumping decreases. This is because the length of the stack becomes shorter and the suspension experiences smaller total frictional drag from the stack walls. Notably, the fractional energy loss is below $\varepsilon_{pump} \leq 0.1\%$ for electrodes used in semi-solid flow battery (black circle symbol, LTP–LFP[4]) and semi-solid hybrid flow batteries (triangle symbol, Li–$S^a$,[25] Li–$S^b$,[45] Li–S/LiI[3]). This estimation is also in agreement with previous work.[49] For semi-solid flowable electrodes with yield stresses of ∼200 Pa that are formulated in this study, power densities of higher than 10 mW $cm_{geo.}^{-2}$ need to be achieved in order to minimize energy losses due to pumping to less than $\varepsilon_{pump} \leq 1\%$ (green circle symbol). The following section highlights how power densities in the range of 16.6 to 159 mW $cm_{geo.}^{-2}$ are achieved in our system.

### Electrochemical evaluation of semi-solid flow electrodes in static cells

Even above the percolation threshold of the acetylene black (AB) dispersed in catholyte ($\Phi$ > 2.5 vol% in Fig. 2b), the discharge voltage, discharge capacity and coulombic efficiency of static cells (Fig. 4a), were influenced greatly by the volume percentage of AB (2.5 to 6.1 vol% of AB) in the 0.7 vol% $Ni(OH)_2$ catholyte (Fig. 4b, c and S4†). The voltage and coulombic efficiencies increased from 50.5 to 87.0% and from 34.7 to 82.6% with increasing volume percentages of AB as shown in Fig. 4c, but no

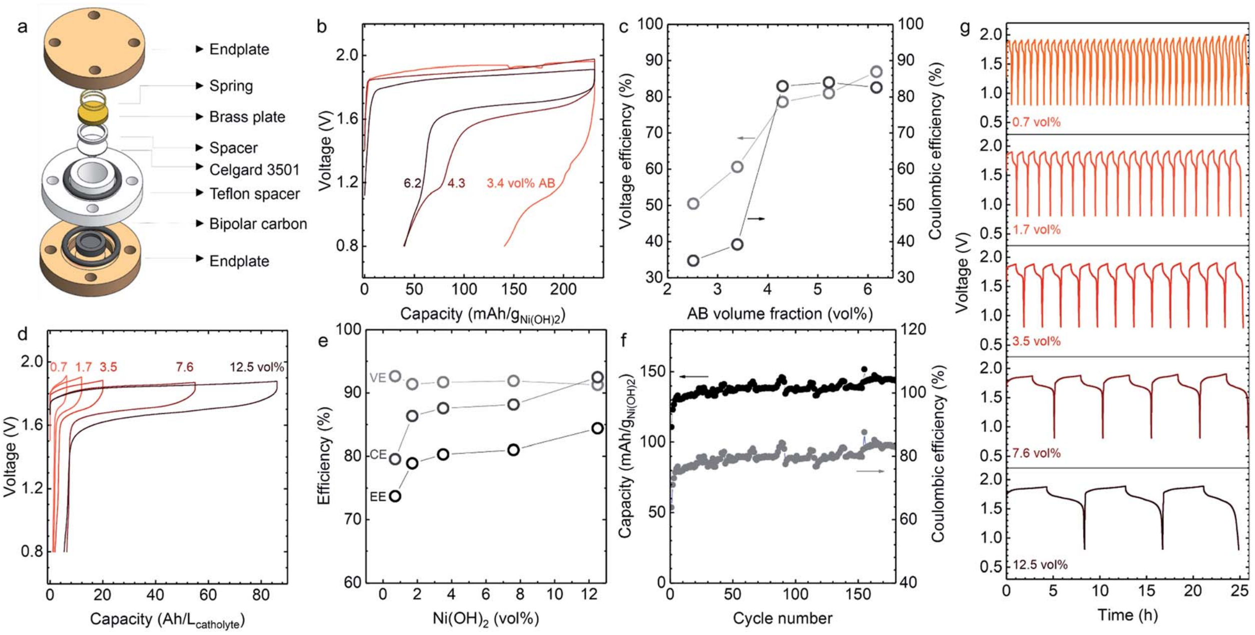

Fig. 4 The electrochemical performance of Zn–Ni semi-solid static cells. (a) Schematic of the structure of the semi-solid static cell. The thickness and geometric area of both catholyte and anolyte in the static cell are 1 mm and 1.1 $cm_{geo.}^2$, respectively. (b) The charge/discharge profiles and (c) the corresponding voltage (grey circles in c) and coulombic efficiencies (black circles in c) of Zn–Ni semi-solid cells with different AB volume percentages (2.5, 3.4, 4.3, 5.2, and 6.1 vol%) + 0.7 vol% $Ni(OH)_2$ catholyte in semi-solid static cells. Here 3.2 vol% of ZnO and 22.5 vol% of Zn was used as the anolyte. (d and e) The charge–discharge profiles and (e) the corresponding voltage (VE), coulombic (CE) and energy efficiencies (EE = VE × CE) of the Zn–Ni semi-solid static cells with anolyte of 5.2 vol% of ZnO and different catholytes containing 5.4–6.1 vol% AB and various volume percentages of $Ni(OH)_2$ (0.7, 1.7, 3.5, 7.6, and 12.5 vol%). The applied current was 2 mA $cm_{geo.}^{-2}$ and the charge capacity was set as 60% SOC based on catholyte. The energy efficiency increased from 73.7 to 84.4% with increase in $Ni(OH)_2$ volume percentages. The coulombic efficiencies for these static cells are ~80% (0.7 vol%), ~87% (1.7 vol%), ~90% (3.5 vol%), ~89%(7.6 vol%), ~94% (12.5 vol%). (f) Cycling stability measurements of Zn–Ni semi-solid static cell with 0.7 vol% $Ni(OH)_2$ + 6.1 vol% AB catholyte and 5.2 vol% ZnO + 22.5 vol% Zn anolyte. The applied current was 1 mA $cm_{geo.}^{-2}$. The charge capacity was limited to 60% SOC. (g) The cycling stability measurements of the Zn–Ni semi-solid static cell containing catholyte with 0.7, 1.7, 3.5, 7.6, and 12.5 vol% $Ni(OH)_2$ (details in Table S4†) and 5.2 vol% ZnO + 22.0 vol% Zn anolyte. The applied current was 2 mA $cm_{geo.}^{-2}$. The charge capacity was limited to 60% SOC. Cu mesh (100 × 100) was used in the anode for even distribution of Zn plating during the charging process. All of these charge/discharge curves were collected after one activation cycle with 120% SOC as described in ESI.†

significant change was noted at AB volume percentages greater than 4.3 vol%. Here, the volume percentages of Zn (22.5 vol%) and ZnO (3.2 vol%) in the anolyte were kept constant to ensure the discharge voltage, discharge capacity and coulombic efficiency are not limited by the anolyte. At this composition, the ohmic resistance from the Zn/ZnO anolyte (Fig. 2a) was much smaller than that from the $Ni(OH)_2$ catholyte (Fig. 2b) and the discharge capacity of Zn/ZnO anode is around 100 times higher than the studied $Ni(OH)_2$ catholytes.

As the $Ni(OH)_2$ equilibrium potential (1.46 V *vs.* RHE, Fig. S1†) is higher than the oxygen evolution reaction (OER) potential (~1.23 V *vs.* RHE), parasitic reactions such as OER[50,51] can contribute more to the charging capacity when AB volume percentages are low, leading to much smaller discharge capacities and coulombic efficiencies. With high AB volume percentages (>4.3 vol%), the ability to disperse more $Ni(OH)_2$ particles and reduction in OER contributes to the larger charging capacity, leading to greater rechargeability of Zn–Ni semi-solid batteries. In addition, we determined that AB volume percentages greater than 5.2 vol% were needed for stable cycling (Fig. S5†). To further understand the stability of the catholyte during cycling, we conducted a series of electrochemical impedance spectroscopy (EIS) measurements (Fig. S6†) at the end of different cycles. The resistance of semi-solid cells containing 4.3 vol% AB increased more rapidly with the number of cycles than a cell with 6.2 vol% AB, which indicates the better mechanical and electrochemical stability of catholyte with increasing AB volume fractions. The increased resistance (shown in Fig. S6† in the intermediate to low frequency range) arises mainly from electric, ionic, and charge transfer resistance, which originates from the lower contact area between $Ni(OH)_2$ and AB in catholytes with lower-volume percentages of dispersed carbon black.[52]

The charge–discharge voltage profiles at 60% SOC (based on the theoretical capacity of $Ni(OH)_2$) for different volume percentages of $Ni(OH)_2$ catholytes from 0.7 to 12.5 vol% are shown in Fig. 4d, with similar volume percentages of AB (5.4–6.1 vol%). The results show a linear increase of discharge capacity with an increasing volume percentage of $Ni(OH)_2$. With a catholyte formulated from 12.5 vol% $Ni(OH)_2$/5.4 vol% AB, the output energy density could reach 134 W h $L_{catholyte}^{-1}$, which is approximately three-fold larger than that of VRFB (~40 W h

$L_{catholyte}^{-1}$).[10] Normalizing charge and discharge capacities by the mass of $Ni(OH)_2$ revealed comparable voltage profiles and slightly increased gravimetric discharge capacities for these semi-solid electrodes (Fig. S7†), and higher coulombic efficiencies (from 83.8% for 0.7 vol% $Ni(OH)_2$ to 93.8% for 12.5 vol% $Ni(OH)_2$ in Fig. 4e). This can be attributed to the increasing contributions to charge capacities from the oxidation of $Ni(OH)_2$ instead of oxygen evolution reactions. The presence of OER during charging agrees with the CV measurements, showing the ratio of reduction to oxidation charge to be ~86% in Fig. S8.† The oxidation of $Ni(OH)_2$ upon charging was evidenced from XRD measurements (Fig. 5a), which showed that $Ni(OH)_2$ peaks became smaller upon charging and largely diminish after 100% SOC (with only ~18% of $Ni(OH)_2$ remaining based on the change of the (100) peak intensity).[53] The presence of 5 wt% CoO in $Ni(OH)_2$ provides a conductive network by forming conductive CoOOH (indicated by CoOOH (003) and (015) peaks in Fig. 3a) as suggested in previous work.[54–57] Further support came from Ni L-edge XANES spectra of different charging states of the cathode with 12.5 vol% $Ni(OH)_2$ and 5.4 vol% AB, where data is collected from total-electron yield (TEY) (Fig. 5b). The high ratio of $L_{3,high}$ (854.8 eV)/$L_{3,low}$ (852.7 eV) in Fig. 5c indicates the high oxidation state of Ni in the cathode. Increasing from 60% to 100% SOC, the slope of oxidation begins to flatten, indicating the presence of more parasitic reactions in 100% SOC. Also, compared to the ratio of $L_{3,high}$ (854.8 eV)/$L_{3,low}$ (852.7 eV) for the $LiNi^{3+}O_2$ [58] shown in Fig. 5c, the $Ni(OH)_2$ cathode after 100% SOC is still quite low, which is further indication of parasitic reactions. Both XRD and XANES results suggest the charge–discharge scenario for Zn–Ni semi-solid battery should be limited by the $Ni(OH)_2$ capacity (<60% theoretical SOC) to lower the impact of parasitic reactions (OER).[50,51]

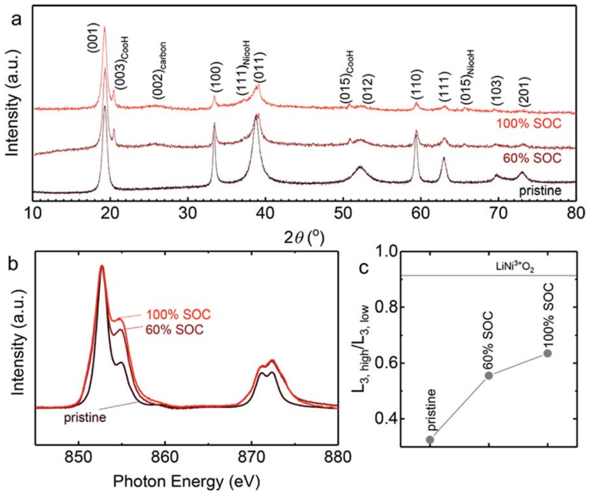

Fig. 5 (a) The normalized XRD patterns of $Ni(OH)_2$ before (pristine) and after charge with 60% and 100% SOC. The peak at ~19° is a characteristic peak of both β-NiOOH and $Ni(OH)_2$. The intensity of other characteristic peaks of $Ni(OH)_2$ decreases with increase of SOC, indicating the oxidation of $Ni(OH)_2$ during charging. (b) *Ex situ* Ni L3/2-edge XANES spectra of pristine $Ni(OH)_2$, 60% SOC, and 100% SOC samples using total-electron yield (TEY) mode. The spectra were normalized at 852.7 eV. (c) The oxidation states of $Ni(OH)_2$ during the charging process using the ratio of $L_{3,high}$ (854.8 eV)/$L_{3,low}$ (852.7 eV). Lithium nickelate ($LiNi^{3+}O_2$) from previously-reported work[58] were used as the reference for $Ni^{3+}$. The dried semi-solid catholyte used in XRD and XANES measurements was charged 12.5 vol% $Ni(OH)_2$ and 5.4 vol% AB, which was paired with anolyte 22.0 vol% Zn and 5.2 vol% ZnO. The cells were charged galvanostatically at 2.0 mA $cm_{geo.}^{-2}$.

In summary, a high power density up to 159 mW $cm_{geo.}^{-2}$ (average discharge voltage ~1.3 V) was obtained for the Zn–Ni semi-solid electrodes in the static cell. A semi-solid static battery containing catholyte with 12.5 vol% $Ni(OH)_2$ and 5.4 vol% AB, plus an anolyte with 5.2 vol% ZnO and 22.0 vol% Zn was selected for the rate capability studies, and the charge capacity was set as 40% SOC. The charge and discharge voltage profiles at different current densities (2, 10, 20, 30, 40, and 50 mA $cm_{geo.}^{-2}$) are shown in Fig. S9,† from which power densities up to 79 mW $cm_{geo.}^{-2}$ (average discharge voltage ~1.6 V, energy density 44 W h $L_{catholyte}^{-1}$) could be obtained. Decreasing the volume percentage of $Ni(OH)_2$ led to greater power density being obtainable from Zn–Ni semi-solid batteries. For example, the catholyte of 7.6 vol% $Ni(OH)_2$ (corresponding to a theoretical capacity of 150 W h $L_{catholyte}^{-1}$ for discharge voltage of 1.7 V) showed power densities up to 159 mW $cm_{geo.}^{-2}$ (average discharge voltage ~1.3 V, energy density 31 W h $L_{catholyte}^{-1}$) (Fig. S10†), which offered power densities comparable to those of VRFBs (~100 mW $cm_{geo.}^{-2}$, ~40 W h $L_{catholyte}^{-1}$)[12] and Zn–$I_2$[a] (~90 mW $cm_{geo.}^{-2}$, 156 W h $L_{catholyte}^{-1}$)[38] but much greater than Li–S (~10 mW $cm_{geo.}^{-2}$)[25] as shown in Fig. 6.

The Zn–Ni semi-solid battery shows high cycling stability as shown in Fig. 4f, where steady discharge capacity and coulombic efficiency were observed for catholyte with 0.7 vol% $Ni(OH)_2$ and 6.2 vol% AB and anolyte with 5.2 vol% ZnO and 22.0 vol% Zn up to 180 cycles. The coulombic efficiency (CE) of

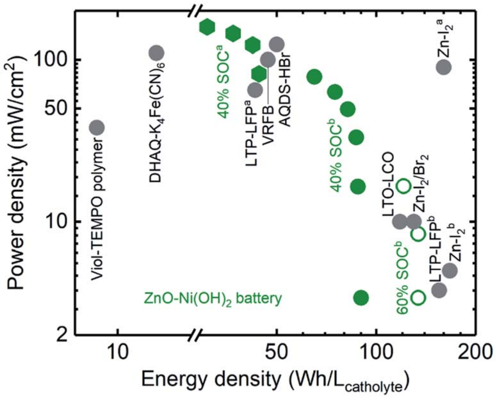

Fig. 6 Ragone plot of static semi-solid battery (ZnO–$Ni(OH)_2$) and reported redox flow battery chemistry including Viol–TEMPO polymer,[63] DHAQ–$K_4Fe(CN)_6$,[14] AQDS–HBr,[9] LTO–LCO,[26] LTP–LFP[a],[4] LTP–LFP[b],[62] VRFB,[12] Zn–$I_2/Br_2$,[35] Zn–$I_2$[a],[38] and Zn–$I_2$[b].[61] The Zn–Ni semi-solid battery chemistry shown from this work contains anolyte with 5.2 vol% ZnO and catholyte with 7.6 (green hexagon, 40% SOC[a]) and 12.5 vol% $Ni(OH)_2$ (green solid 40% SOC[b] and open circles 60% SOC[b]). Abbreviations: AQDS: 9,10-anthraquinone-2,7-disulphonic acid, DHAQ: 2,6-dihydroxyanthraquinone, TEMPO: 2,2,6,6-tetramethylpiperidinyloxyl, Viol: viologen, LTP: $LiTi_2(PO_4)_3$, LFP: $LiFePO_4$, LTO: $Li_4Ti_5O_{12}$.

<80% could be attributed to the parasitic OER, which became less prominent with increasing $Ni(OH)_2$ volume percentage. The catholyte could be cycled with minimum loss and with greater coulombic efficiencies maintained at ~90% (data shown for 1.7, 3.5, 7.6, and 12.5 vol% of $Ni(OH)_2$ in Fig. 4h). These values are much higher than for a previously-reported Zn–Ni semi-solid flow battery (<80% of CE).[28] The greater electrochemical reversibility and stability of $Ni(OH)_2$ semi-solid electrodes (Fig. 4f) can be attributed to the mechanical stability of the semi-solid electrodes (Fig. 3c and d), and to the lesser importance of parasitic OER during cycling. The discharge capacity was found to remain relatively stable over 180 cycles, with a slight increase in the first several cycles (~5 cycles), as shown in Fig. 4f and S11a.† From the 5th to 100th cycle in Fig. S11b,† there is no drastic change in the charge–discharge voltage profile nor discharge capacity, except for the increased overpotentials. Going beyond the 100th to 180th cycle (Fig. S11b†), we note the appearance of a small discharge plateau around 1.0 V. According to previous work,[59] the second discharge plateau at ~1.0 V can be assigned to the reduction of γ-NiOOH to β-$Ni(OH)_2$. The formation of γ-NiOOH may come from the overcharging of β-$Ni(OH)_2$ during the cycling process[59] and/or the cell drying out during cycling (180 cycles translating to 180 hours). Additional optimization involving reducing the upper voltage limit, and increasing the lower voltage limit to 1.2 V (as negligible capacities are found below 1.2 V) as well as developing static cells with much improved hermetic seals is needed to further increase cycling stability. During post-mortem characterization, we observed the particle morphology of $Ni(OH)_2$ remained largely unchanged after cycling. However, we observed that the surface of $Ni(OH)_2$ particles developed plate-like structures after 20 cycles (Fig. S12d†), similar to the ones observed after 180 cycles (Fig. S12f†). Also, in this study, we did not observe any formation of Zn dendrites, which can be attributed to the much greater true Zn surface area per geometric electrode area for our Zn semi-solid anolyte than for a Zn plate. For example, a Zn suspension (with 23 vol% of particles with an average size of 50 μm, 328 $\mathrm{mg_{Zn}\ cm_{geo.}^{-2}}$) filled into a 2 mm channel, provides 55 times larger true surface area of Zn than the geometric electrode area, or the corresponding Zn plate where the true Zn surface area is estimated to be the same as the geometric electrode area of Zn plate. The current density required for Zn dendrite formation within a given time can be estimated from Sand's relationship,[60] which is expressed in terms of the current density required for diffusion limited plating that causes formation of dendrites. If dendrites were to form at 0.5 mA $\mathrm{cm_{geo.}^{-2}}$ (or 0.5 mA $\mathrm{cm_{zn}^{-2}}$) within 1 hour for a planar electrode,[60] it would take 28 mA $\mathrm{cm_{geo.}^{-2}}$ (0.5 mA $\mathrm{cm_{zn}^{-2}}$) for dendrites to develop on the Zn surface within the same time, suggesting the formation of dendrites can be more readily suppressed for Zn semi-solid electrodes than Zn plate electrodes.

Table 1 The physical properties and performance summary of the Zn–Ni semi-solid cell with the highest achieved energy density

| | | |
|---|---|---|
| $Ni(OH)_2$/AB catholyte[a] yield stress | Pa | 209 |
| ZnO/Zn anolyte[b] yield stress | Pa | 222 |
| $Ni(OH)_2$/AB catholyte[a] conductivity | $\mathrm{mS\ cm^{-1}}$ | 0.9 |
| ZnO/Zn anolyte[b] conductivity | $\mathrm{mS\ cm^{-1}}$ | 48.9 |
| Energy density | $\mathrm{W\ h\ L_{catholyte}^{-1}}$ | 134 |
| Energy efficiency | % | 84.4 |

[a] 12.5 vol% $Ni(OH)_2$, 5.4 vol% AB, 0.7 vol% Carbopol 940, and 81.3 vol% KOH solution. [b] 5.2 vol% ZnO, 22 vol% Zn, 0.8 vol% of Carbopol, 72.0 vol% KOH solution.

We have been able to design semi-solid electrodes with an energy density of up to 134 $\mathrm{W\ h\ L_{catholyte}^{-1}}$ and power density of up to 159 mW $\mathrm{cm_{geo.}^{-2}}$ using Zn–Ni chemistry in static cells (the physical properties of these semi-solid electrodes are detailed in Table 1). These semi-solid electrodes can be quantitatively compared with other chemistries reported previously in a Ragone plot, as shown in Fig. 6. By increasing the SOC of the catholyte containing 12.5 vol% of $Ni(OH)_2$ from 40% (green solid dots) to 60% (green open circles), the energy densities increase up to 134 $\mathrm{W\ h\ L_{catholyte}^{-1}}$, which is comparable with previous works like Zn–$I_2$/$Br_2$,[35] Zn–$I_2$[b],[61] and LTP–LFP[b].[62] To further increase the power densities, we used catholyte with a lower volume fraction of $Ni(OH)_2$ (7.6 vol%), which can achieve a power density of up to 159 mW $\mathrm{cm_{geo.}^{-2}}$, which becomes comparable to values reported for VRFB[29] and Zn–$I_2$[a].[38] When compared to organic molecules- or polymeric-based electrolytes (DHAQ–$K_4Fe(CN)_6$,[14] AQDS–HBr,[9] Viol–TEMPOpolymers,[63]) these Zn–Ni semi-solid electrodes show much higher energy and power densities. Although we have compared various flow battery chemistries in the Ragone plot, it is worth noting that the Ragone plot does not incorporate information such as maximum number of cycles achieved or capacity retention. Unlike all-liquid flow batteries, an SSFB has an advantage of no species cross-over, because the solid particles are too large to penetrate through the separator. Hence, if the redox couple is cyclable in a conventional solid battery, they should be cyclable in SSFB too. The high energy and power densities (Fig. 6), high coulombic efficiency (Fig. 4e) and the low pumping energy loss (Fig. 3e) of the ZnO and $Ni(OH)_2$ semi-solid electrodes developed in the present work makes a promising combination to be studied in a flow cell system.

### Zn–Ni semi-solid flow battery performance

To illustrate this potential, we have also conducted preliminary tests of these semi-solid electrodes in a specially designed 3D-printed geometry to show the feasibility of the flow battery concept. The schematic design and a photo of the assembled flow cell are shown in Fig. 7a and b, respectively. The rechargeability of Zn–Ni semi-solid electrodes in the flow cell was examined in an intermittent mode, in which the electrodes were flowed in at 0.2 mL $\mathrm{min^{-1}}$. Unlike all-liquid flow batteries which require high flow rates (10–40 mL $\mathrm{min^{-1}}$)[64] to compensate for the inherent mass transport limitation,[64] electrically conductive semi-solid electrodes can be operated at low flow rates or even static or intermittent conditions.[65] In addition, operating at low flow rates (corresponding in dimensionless terms to high Bingham numbers, Bn > 50) has other advantages such as better flow uniformity.[66] Moreover, as suggested by previous work (see

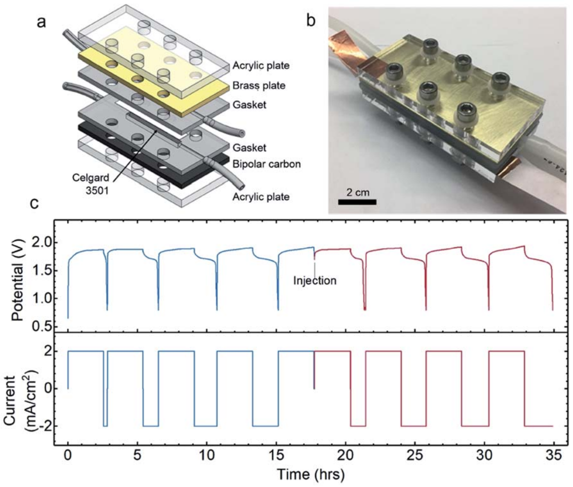

Fig. 7 (a) The schematic 3D structure of flow cell. The effective channel geometric area is 1.2 cm$^2$ (0.3 × 4.0 cm). The thickness of the flow channel is 3 mm. (b) A photograph of the assembled flow cell setup. (c) Galvanostatic charge–discharge performance of Ni–Zn semi-solid flow battery with 3.5 vol% $Ni(OH)_2$ and 5.9 vol% AB catholyte and 5.2 vol% ZnO and 22 vol% Zn anolyte. The applied current was 2 mA cm$^{-2}$. The suspensions were pumped in batches at 0.2 mL min$^{-1}$.

for example Duduta *et al.*[26] and Smith *et al.*[66]), intermittent flow operation can be less energy-intensive for pumping. Previous experimental studies have reported that the electronic conductivity of well-percolated carbon black suspensions at high shear rates is usually maintained at the same order of magnitude as measured in samples at vanishingly low shear rates.[32,41] Because the suspensions used in SSFB are usually operated at very low flow rates (corresponding to Bingham numbers, Bn > 50),[66] one may expect the bulk of the suspension remains unsheared during flow,[62] thus maintaining its electronic conductivity at the values measured under static equilibrium conditions.

After a few initial formation cycles (4 cycles) to activate the $Ni(OH)_2$,[67] the first batch of electrodes were charged and then displaced by injecting a new batch of Zn and $Ni(OH)_2$ semi-solid electrodes into the anolyte and catholyte compartments, respectively. The anolyte was composed of 22 vol% Zn and 5.2 vol% ZnO, while the catholyte was composed of 5.4 vol% AB and 2.9 vol% $Ni(OH)_2$. Identical charge–discharge profiles were found for the first and second batches (Fig. 7c), where both exhibited 23 W h $L_{catholyte}^{-1}$, and 72 and 80% coulombic efficiency respectively in the fully activated cycle. Post-mortem XRD and SEM analysis of the $Ni(OH)_2$ catholyte (with the same composition as that used in Fig. 7) after 10 cycles in the static cell was conducted (Fig. S13†). XRD measurements of the $Ni(OH)_2$ catholyte in the discharged state after 10 cycles revealed peaks similar to that of pristine catholyte plus additional ZnO peaks, which can be attributed to the cross-over of soluble Zn-containing species such as $Zn(OH)_4^{2-}$ from the ZnO/Zn anolyte during cycling. In addition, the spherical shape of $Ni(OH)_2$ particles remained unchanged after cycling (Fig. S12a and S13b†).

These results show the possibility of utilizing cheap, safe and high energy density suspensions to formulate flowable electrodes for semi-solid flow battery applications. A similar technique can be used to maximize the utilization of other active materials based on aqueous chemistry (*e.g.* Prussian Blue analogues,[68] manganese oxides,[69] iron oxides[70]) as a flowable electrode in flow battery applications. Our calculation suggests that the mechanical energy dissipation due to pumping is small (<1% of total battery output) within the flow battery stack. However, there is still further work needed to commercialize this technology. For example, enhancing phase stability of suspensions during strong shearing flow in thin channels.[71,72] On the electrochemistry side, although the Zn semi-solid electrode is a promising material as an anolyte for aqueous chemistry, there are still some unresolved issues concerning its cyclability. For example, possibly higher conductivity near the current collector than in the center of the suspension, and poor distribution of zincate ion at high current rates[73] could cause nonuniform Zn plating process (Fig. S14†). A separate comprehensive study is needed to design the anolyte and the corresponding flow battery configuration to enhance its stability and reversibility.

## Conclusions

We have developed ZnO and $Ni(OH)_2$ flowable electrodes with high power and energy densities and negligible energy loss during pumping for Zn–Ni semi-solid flow battery (SSFB), by combining both electrochemistry knowledge and understanding of the rheology of semi-solid electrodes (a high-volume fraction suspension). Firstly, mechanically-stable semi-solid electrodes were designed and characterized using a polymeric microgel (Carbopol©) dispersed in 7 M KOH electrolyte to generate a yield stress that supports electronically-conductive dense suspensions. These slurries were formulated respectively from conductive Zn particles with active colloidal ZnO particles in the anolyte and conductive colloidal carbon black (AB) with $Ni(OH)_2$ particles in the catholyte. Subsequently, conductive suspensions containing 6.2 vol% of carbon and 23.1 vol% of Zn respectively have been used as base systems for preparing catholytes and anolytes containing different volume percentages of active materials which are conductively percolated and show high voltage efficiency and high coulombic efficiency. Both of these semi-solid electrode formulations exhibited non-Newtonian flow behaviour with a yield stress of ∼200 Pa which assists in stability against sedimentation. Electrochemical tests were performed in specially-designed static and flow cells. High energy densities up to 134 W h $L_{catholyte}^{-1}$ with coulombic efficiencies up to ∼94% and power densities up to 159 mW $cm_{geo.}^{-2}$ have been achieved in semi-solid electrodes with carefully-formulated suspensions in static cells. Our calculations suggest that the high power density and reasonable yield stress of the semi-solid electrode developed in this study guarantees pumping energy loss of less than 1% of the discharged energy of the battery. The high coulombic efficiency and low parasitic loss can be attributed to the optimized charging protocol. By limiting the charging capacity to 60%

SOC, we have been able to show through X-ray diffraction and XANES analysis of the charged catholytes that the oxidation of $Ni(OH)_2$ is the predominant oxidation reaction instead of oxygen evolution reactions. When compared with other aqueous systems, the Zn–Ni semi-solid flow battery system developed here has promising energy and power densities. This newly-designed aqueous Zn–Ni semi-solid flow battery paves a way to develop environmentally friendly and cost-effective energy storage systems for stationary applications.

## Conflicts of interest

There are no conflicts to declare.

## Acknowledgements

This work is supported by Eni. Research described in this paper Ni L-edge XANES spectra were collected at the Canadian Light Source, which is supported by the University of Saskatchewan, the Government of Saskatchewan.

## Notes and references

1 M. K. Gunnar Boye Olesen and E. Lebre la Rovere, *Sustainable Energy Vision 2050*, http://www.inforse.org/europe/VisionWorld.htm.
2 S. Becker, B. A. Frew, G. B. Andresen, T. Zeyer, S. Schramm, M. Greiner and M. Z. Jacobson, *Energy*, 2014, **72**, 443–458.
3 H. Chen and Y.-C. Lu, *Adv. Energy Mater.*, 2016, **6**, 1502183.
4 Z. Li, K. C. Smith, Y. Dong, N. Baram, F. Y. Fan, J. Xie, P. Limthongkul, W. C. Carter and Y.-M. Chiang, *Phys. Chem. Chem. Phys.*, 2013, **15**, 15833–15839.
5 T. M. I. Mahlia, T. J. Saktisahdan, A. Jannifar, M. H. Hasan and H. S. C. Matseelar, *Renewable Sustainable Energy Rev.*, 2014, **33**, 532–545.
6 B. Dunn, H. Kamath and J.-M. Tarascon, *Science*, 2011, **334**, 928–935.
7 M. L. Perry and A. Z. Weber, *J. Electrochem. Soc.*, 2016, **163**, A5064–A5067.
8 Q. Huang and Q. Wang, *ChemPlusChem*, 2014, **80**, 312–322.
9 B. Huskinson, M. P. Marshak, C. Suh, S. Er, M. R. Gerhardt, C. J. Galvin, X. Chen, A. Aspuru-Guzik, R. G. Gordon and M. J. Aziz, *Nature*, 2014, **505**, 195.
10 M. Skyllas-Kazacos, C. Menictas and M. Kazacos, *J. Electrochem. Soc.*, 1996, **143**, L86–L88.
11 G. L. Soloveichik, *Chem. Rev.*, 2015, **115**, 11533–11558.
12 L. Li, S. Kim, W. Wang, M. Vijayakumar, Z. Nie, B. Chen, J. Zhang, G. Xia, J. Hu and G. Graff, *Adv. Energy Mater.*, 2011, **1**, 394–400.
13 M. Park, J. Ryu, W. Wang and J. Cho, *Nat. Rev. Mater.*, 2016, **2**, 16080.
14 K. Lin, Q. Chen, M. R. Gerhardt, L. Tong, S. B. Kim, L. Eisenach, A. W. Valle, D. Hardee, R. G. Gordon and M. J. Aziz, *Science*, 2015, **349**, 1529–1532.
15 D. G. Kwabi, K. Lin, Y. Ji, E. F. Kerr, M.-A. Goulet, D. De Porcellinis, D. P. Tabor, D. A. Pollack, A. Aspuru-Guzik, R. G. Gordon and M. J. Aziz, *Joule*, 2018, **2**, 1894–1906.
16 E. S. Beh, D. De Porcellinis, R. L. Gracia, K. T. Xia, R. G. Gordon and M. J. Aziz, *ACS Energy Lett.*, 2017, **2**, 639–644.
17 A. Hollas, X. Wei, V. Murugesan, Z. Nie, B. Li, D. Reed, J. Liu, V. Sprenkle and W. Wang, *Nat. Energy*, 2018, **3**, 508–514.
18 C. Jia, F. Pan, Y. G. Zhu, Q. Huang, L. Lu and Q. Wang, *Sci. Adv.*, 2015, **1**, e1500886.
19 Y. G. Zhu, Y. Du, C. Jia, M. Zhou, L. Fan, X. Wang and Q. Wang, *J. Am. Chem. Soc.*, 2017, **139**, 6286–6289.
20 Y. Chen, M. Zhou, Y. Xia, X. Wang, Y. Liu, Y. Yao, H. Zhang, Y. Li, S. Lu, W. Qin, X. Wu and Q. Wang, *Joule*, 2019, **3**, 2255–2267.
21 M. Zhou, Y. Chen, Q. Zhang, S. Xi, J. Yu, Y. Du, Y.-S. Hu and Q. Wang, *Adv. Energy Mater.*, 2019, **9**, 1901188.
22 M. Skyllas-Kazacos, *ECS Trans.*, 2019, **89**, 29–45.
23 M. Duduta, B. Ho, V. C. Wood, P. Limthongkul, V. E. Brunini, W. C. Carter and Y. M. Chiang, *Adv. Energy Mater.*, 2011, **1**, 511–516.
24 T.-S. Wei, F. Y. Fan, A. Helal, K. C. Smith, G. H. McKinley, Y.-M. Chiang and J. A. Lewis, *Adv. Energy Mater.*, 2015, **5**, 1500535.
25 H. Chen, Q. Zou, Z. Liang, H. Liu, Q. Li and Y.-C. Lu, *Nat. Commun.*, 2015, **6**, 5877.
26 M. Duduta, B. Ho, V. C. Wood, P. Limthongkul, V. E. Brunini, W. C. Carter and Y.-M. Chiang, *Adv. Energy Mater.*, 2011, **1**, 511–516.
27 Z. Li, M. S. Pan, L. Su, P.-C. Tsai, A. F. Badel, J. M. Valle, S. L. Eiler, K. Xiang, F. R. Brushett and Y.-M. Chiang, *Joule*, 2017, **1**, 306–327.
28 J. Liu and Y. Wang, *J. Power Sources*, 2015, **294**, 574–579.
29 W. Lu, Z. Yuan, M. Li, X. Li, H. Zhang and I. Vankelecom, *Adv. Funct. Mater.*, 2017, **27**, 1604587.
30 R. B. Bird, R. C. Armstrong and O. Hassager, *Dynamics of Polymeric Liquids: Fluid Mechanics*, Fluid Mechanics, 1987, vol. 1.
31 D. Bonn, M. M. Denn, L. Berthier, T. Divoux and S. Manneville, *Rev. Mod. Phys.*, 2017, **89**, 035005.
32 A. Helal, T. Divoux and G. H. McKinley, *Phys. Rev. Appl.*, 2016, **6**, 064004.
33 Y. Zeng, T. Zhao, L. An, X. Zhou and L. Wei, *J. Power Sources*, 2015, **300**, 438–443.
34 Q. Lai, H. Zhang, X. Li, L. Zhang and Y. Cheng, *J. Power Sources*, 2013, **235**, 1–4.
35 G.-M. Weng, Z. Li, G. Cong, Y. Zhou and Y.-C. Lu, *Energy Environ. Sci.*, 2017, **10**, 735–741.
36 P. Zhao, H. Zhang, H. Zhou and B. Yi, *Electrochim. Acta*, 2005, **51**, 1091–1098.
37 J. F. Parker, C. N. Chervin, I. R. Pala, M. Machler, M. F. Burz, J. W. Long and D. R. Rolison, *Science*, 2017, **356**, 415–418.
38 C. Xie, Y. Liu, W. Lu, H. Zhang and X. Li, *Energy Environ. Sci.*, 2019, **12**, 1834–1839.
39 K. B. Hatzell, J. Eller, S. L. Morelly, M. H. Tang, N. J. Alvarez and Y. Gogotsi, *Faraday Discuss.*, 2017, **199**, 511–524.
40 G. Shukla, D. del Olmo Diaz, V. Thangavel and A. A. Franco, *ACS Appl. Mater. Interfaces*, 2017, **9**, 17882–17889.
41 H. Parant, G. Muller, T. Le Mercier, J. Tarascon, P. Poulin and A. Colin, *Carbon*, 2017, **119**, 10–20.

42 V. Trappe, V. Prasad, L. Cipelletti, P. N. Segre and D. A. Weitz, *Nature*, 2001, **411**, 772.

43 V. Litvinov and P. Steeman, *Macromolecules*, 1999, **32**, 8476–8490.

44 A. N. Beris, J. Tsamopoulos, R. C. Armstrong and R. Brown, *J. Fluid Mech.*, 1985, **158**, 219–244.

45 F. Y. Fan, W. H. Woodford, Z. Li, N. Baram, K. C. Smith, A. Helal, G. H. McKinley, W. C. Carter and Y.-M. Chiang, *Nano Lett.*, 2014, **14**, 2210–2218.

46 X. Chen, B. J. Hopkins, A. Helal, F. Y. Fan, K. C. Smith, Z. Li, A. H. Slocum, G. H. McKinley, W. C. Carter and Y.-M. Chiang, *Energy Environ. Sci.*, 2016, **9**, 1760–1770.

47 M. Cloitre and R. T. Bonnecaze, *Rheol. Acta*, 2017, **56**, 283–305.

48 A. Yoshimura and R. K. Prud'homme, *J. Rheol.*, 1988, **32**, 53–67.

49 B. J. Hopkins, K. C. Smith, A. H. Slocum and Y.-M. Chiang, *J. Power Sources*, 2015, **293**, 1032–1038.

50 Y. Li, C. He, E. V. Timofeeva, Y. Ding, J. Parrondo, C. Segre and V. Ramani, *Front. Energy*, 2017, **11**, 401–409.

51 M. Morishita, S. Ochiai, T. Kakeya, T. Ozaki, Y. Kawabe, M. Watada, S. Tanase and T. Sakai, *Electrochemistry*, 2008, **76**, 802–807.

52 T. J. Petek, N. C. Hoyt, R. F. Savinell and J. S. Wainright, *J. Electrochem. Soc.*, 2016, **163**, A5001–A5009.

53 C. Léger, C. Tessier, M. Ménétrier, C. Denage and C. Delmas, *J. Electrochem. Soc.*, 1999, **146**, 924–932.

54 M. Oshitani, H. Yufu, K. Takashima, S. Tsuji and Y. Matsumaru, *J. Electrochem. Soc.*, 1989, **136**, 1590–1593.

55 V. Pralong, A. Delahaye-Vidal, B. Beaudoin, B. Gerand and J. Tarascon, *J. Mater. Chem.*, 1999, **9**, 955–960.

56 W. Hu, X. Gao, M. Geng, Z. Gong and D. Noreus, *J. Phys. Chem. B*, 2005, **109**, 5392–5394.

57 X.-Z. Fu, Q.-C. Xu, R.-Z. Hu, B.-X. Pan, J.-D. Lin and D.-W. Liao, *J. Power Sources*, 2007, **164**, 916–920.

58 J. Xu, E. Hu, D. Nordlund, A. Mehta, S. N. Ehrlich, X.-Q. Yang and W. Tong, *ACS Appl. Mater. Interfaces*, 2016, **8**, 31677–31683.

59 N. Sac-Epée, M. R. Palacín, B. Beaudoin, A. Delahaye-Vidal, T. Jamin, Y. Chabre and J. M. Tarascon, *J. Electrochem. Soc.*, 1997, **144**, 3896–3907.

60 V. Yufit, F. Tariq, D. S. Eastwood, M. Biton, B. Wu, P. D. Lee and N. P. Brandon, *Joule*, 2019, **3**, 485–502.

61 B. Li, Z. Nie, M. Vijayakumar, G. Li, J. Liu, V. Sprenkle and W. Wang, *Nat. Commun.*, 2015, **6**, 6303.

62 J. Yu, L. Fan, R. Yan, M. Zhou and Q. Wang, *ACS Energy Lett.*, 2018, **3**, 2314–2320.

63 T. Janoschka, N. Martin, U. Martin, C. Friebe, S. Morgenstern, H. Hiller, M. D. Hager and U. S. Schubert, *Nature*, 2015, **527**, 78.

64 Q. Xu and T. Zhao, *Phys. Chem. Chem. Phys.*, 2013, **15**, 10841–10848.

65 N. C. Hoyt, R. F. Savinell and J. S. Wainright, *Chem. Eng. Sci.*, 2016, **144**, 288–297.

66 K. C. Smith, Y.-M. Chiang and W. C. Carter, *J. Electrochem. Soc.*, 2014, **161**, A486–A496.

67 W. K. Zhang, X. H. Xia, H. Huang, Y. P. Gan, J. B. Wu and J. P. Tu, *J. Power Sources*, 2008, **184**, 646–651.

68 B. Wang, Y. Han, X. Wang, N. Bahlawane, H. Pan, M. Yan and Y. Jiang, *iScience*, 2018, **3**, 110–133.

69 H. Pan, Y. Shao, P. Yan, Y. Cheng, K. S. Han, Z. Nie, C. Wang, J. Yang, X. Li and P. Bhattacharya, *Nat. Energy*, 2016, **1**, 16039.

70 D. Lei, D.-C. Lee, E. Zhao, A. Magasinski, H.-R. Jung, G. Berdichevsky, D. Steingart and G. Yushin, *Nano Energy*, 2018, **48**, 170–179.

71 S. Yang, S.-I. Jeon, H. Kim, J. Choi, J.-G. Yeo, H.-R. Park and D. K. Kim, *ACS Sustainable Chem. Eng.*, 2016, **4**, 4174–4180.

72 Z. Varga, V. Grenard, S. Pecorario, N. Taberlet, V. Dolique, S. Manneville, T. Divoux, G. H. McKinley and J. W. Swan, *Proc. Natl. Acad. Sci. U. S. A.*, 2019, **116**, 12193–12198.

73 Q. C. Horn and Y. Shao-Horn, *J. Electrochem. Soc.*, 2003, **150**, A652–A658.